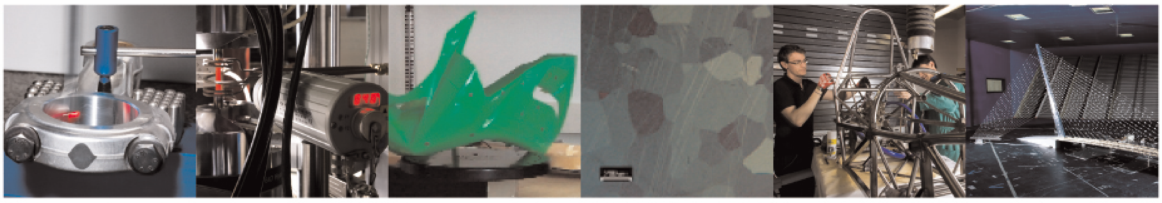

Iterative Reconstruction Method With Auto-Updated Seed Point of Monoscopic Deflectometry for Off-Axis Aspheric

Lan, Menghui;Li, Bing;Wei, Xiang;Zappa, Emanuele

This is a post-peer-review, pre-copyedit version M. Lan, B. Li, X. Wei and E. Zappa, "Iterative Reconstruction Method With Auto-Updated Seed Point of Monoscopic Deflectometry for Off-Axis Aspheric," in IEEE Transactions on Instrumentation and Measurement, vol. 74, pp. 1-12, 2025, Art no. 5038812, doi: 10.1109/TIM.2025.3587357

TIM-25-04769

Iterative reconstruction method with auto-updated seed point of monoscopic deflectometry for off-axis aspheric

Menghui Lan, Bing Li, Xiang Wei, and Emanuele Zappa, *Senior Member, IEEE*

***Abstract*—The complex surface characteristics and misalignment of the geometric and optical axes of off-axis aspherical surfaces pose major challenges in the work to develop a measurement technique that is accurate, effective, and simple. Phase measurement deflectometry (PMD) is a more convenient and cost-effective method than interferometry for measuring specular objects. Nevertheless, monocular PMD necessitates complicated processes or costly additional equipment to resolve height-slope problems, whereas binocular PMD requires more time-consuming matching calculations. In this article, a novel iterative strategy based on monocular PMD technology with an automatic updated seed point during the iterative process is proposed, which only requires an approximate estimation about the height of one point (either, the lowest, middle, or highest) on the measured off-axis aspheric component. The lowest, middle, or highest point of the reconstructed surface is used as the target of auto-updated seed point in the iterative process, and the surface's overall height information is then updated until the difference between two neighboring surface profiles is less than a certain threshold. Finally, the off-axis aspherical surface result is sent out. The proposed monocular PMD method is more straightforward, cost-effective, and simple, requiring only basic and low-cost tools to estimate the initial height of the measured component without the need to obtain the seed point's 3D coordinate. An experiment was performed to evaluate the feasibility and accuracy of the proposed method with the results of high-precision contact measurements as benchmarks. The results also indicated that even the uncertainty in the estimated initial height using common vernier calipers has little effect on the measured surface shape, since it only leads to a small offset in the whole surface location.**

***Index Terms*— Off-axis aspheric, monoscopic deflectometry, auto-updated seed point, iteration**

I. INTRODUCTION

The curvature variations of aspherical surfaces can effectively correct aberration and enhance the quality of imaging. Additionally, they offer the benefits of enhancing the system's relative aperture, expanding the field of view, and reducing the number of optical elements in the system to compensate for the shortcomings of conventional spherical optics. This feature simplifies the system's structure, reduces its weight, and reduces its space occupation. Consequently, they are employed in a variety of fields, including aerospace, space optics, military defense, and high-tech civil applications [1], [2]. Off-axis aspheric are non-rotationally symmetric surfaces that are part of a complete aspheric. They offer supplementary degrees of freedom for the correction of aberrations in the design of optical systems, as their geometric axis is not in alignment with the optical axis [3]. For example, off-axis triple-reflector imaging systems are becoming more widely used in the field of space remote sensing due to their unobstructed nature, large field of view, high signal-to-noise ratios, fewer components, and superior ability to suppress stray light, as compared to coaxial reflector systems in the field of space optics [4]. Furthermore, in the field of large-aperture astronomical telescopes, the fabrication of aspheric reflecting components is frequently accomplished by the technique of combining multiple off-axis aspherical elements. For example, the Thirty Meter Telescope (TMT) utilizes a wide field-of-view adaptive optics system that incorporates active optical co-phase spliced mirrors. The primary mirror of the TMT is a parabolic mirror with a diameter of 30 meters, which is combined with 492 off-axis sub-mirrors that have a diameter of 1.4 meters [5], [6]. Nevertheless, the complex and varied characteristics of optical aspherical surfaces make their processing and measurement significantly more challenging compared to spherical optical elements. As a result, the study of cost-effective, user-friendly, high-precision, and high-efficiency measurement methods has become a prominent area of research in this field [7]. Additionally, the challenge of surface measurement is made greater by the characteristics of off-axis aspherical surfaces, which have geometric axes that do not align with the optical axis.

Conventional aspherical elements lack recognized feature points because their surface is rotationally symmetric. However, an off-axis aspheric is different from a conventional

This work was supported in part by the National Natural Science Foundation of China under Grant 52105482. The work of Menghui Lan was supported by the Politecnico di Milan through China Scholarship Council under Grant 202306280263. (Corresponding author: Menghui Lan)

Menghui Lan is with the State Key Laboratory for Manufacturing System Engineering, Xi’an Jiaotong University, Xi’an 710049, China, and also with the Department of Mechanical Engineering, Politecnico di Milan, 20156 Milan, Italy (e-mail: menghui.lan@stu.xjtu.edu.cn).

Bing Li and Xiang Wei are with the State Key Laboratory for Manufacturing Systems Engineering and the International Joint Laboratory for Micro/Nano Manufacturing and Measurement Technology, Xi’an Jiaotong University, Xi’an 710049, China (e-mail: lb@xjtu.edu.cn, hill_wx@xjtu.edu.cn).

Emanuele Zappa is with the Department of Mechanical Engineering, Politecnico di Milan, 20156 Milan, Italy (e-mail: emanuele.zappa@polimi.it).

aspheric element in that it has a valuable minimum height and a maximum height of an unknown measured surface, and the middle height can be calculated from both. To overcome the disadvantages of complex operations and expensive auxiliary equipment in the monocular PMD technique, as well as the time-consuming nature of the binocular PMD technique, we proposed a novel strategy based on the monocular PMD technique with an auto-updated seed point during the iteration process. The proposed method only requires an approximate estimation about the height of one point (either, the lowest, middle, or highest) on the measured off-axis aspheric component. The iterative process uses the lowest, middle, or highest point of the reconstructed surface as the target of the auto-updated seed point, updating the surface's overall height information until the difference between two neighboring surface profiles is less than a certain threshold. Finally, the off-axis aspherical surface result is sent out. The feasibility of the method is verified by a measurement experiment on an off-axis aspheric. The results also indicated that even the uncertainty in the estimated initial height using common vernier calipers has little effect on the measured surface shape, since it only leads to a small offset in the whole surface location.

II. State of The Art

Surface accuracy measurement for off-axis aspherical surfaces is often categorized into contact and non-contact methods [8]. In contact measurement, which is represented by aspheric profilers, the stylus tip contacts the optical element's surface. The vector height information of all sampling points is then integrated and subtracted from the design value of the surface shape to calculate parameters such as the peak to valley (PV) and root mean square (RMS) value that describe the error of the aspheric surface [9]. Nevertheless, the contact measurement method is slow, the movement mechanism affects the measurement accuracy, which makes it challenging to obtain high-accuracy results, and the contact between the probe and the component's surface can damage the component [10], [11]. In the category of non-contact measuring methods, there are two primary types: interferometry and deflectometry [12], [13]. Interferometry is an optical measurement technique that utilizes light interference to obtain surface shape data from an interference image. It is the primary method for accurately detecting the shape of aspherical surfaces, including both zero-position and non-zero-position measurements [14]. The zero-position measurement approach often utilizes compensating mirrors and computer-generated holograms (CGH) to transform the spherical wavefront into an aspherical wavefront. This makes it possible for the acquisition of the zero-position interference fringe, and the errors of the measured aspherical surface can be determined by analyzing the difference between the actual interference fringe and the ideal interference fringe [15]. Interference detection offers several benefits, including excellent resolution, accuracy, and sensitivity. However, when dealing with aspherical surfaces that have varying surface parameters, custom null optics are required to transform aspherical waves. As a result, the cost of interferometry is high. Alternatively, non-zero measurements that employ sub-aperture splicing do not necessitate specific compensating mirrors; however, they can be more complicated and challenging to operate and manage [16]. Additionally, to enable interferometry of off-axis aspherical surfaces, more intricate optical path designs and modifications are necessary.

Phase measuring deflectometry (PMD), another non-contact measuring technique, is commonly employed for accurate surface shape measurement of specular components due to the advantages of convenience, low cost, and adaptability [17], [18]. The fundamental principle of PMD is that the fringe maps displayed on the screen are reflected and deformed by the measured surface and captured by the camera. The subsequent dephasing process establishes the correspondence between the screen and the camera pixel points, which in turn calculates the slope data at each point of the measured surface. Then surface reconstruction is performed to determine the actual surface [19]. However, the PMD approach suffers from the significant problem of height-slope ambiguity, which many scholars have endeavored to solve in their research. The majority of modern PMDs are performed using monocular techniques with a single camera or binocular strategies with two cameras.

Monocular PMD technology involves a method called direct PMD (DPMD) to solve the issue of height-slope ambiguity. It requires moving the screen or adding a flat beam splitter to create a parallel arrangement of the two LCD panels [20]. Tang et al. measured the 3D profiles of aspherical mirrors using the PMD method, which involved moving the screen and camera separately [21]. This method does not need complicated calibration. However, when factoring in component displacement errors, the physical displacement affects the measurement's accuracy. Therefore, it has stringent requirements for operational accuracy. Su et al. have developed another monocular PMD technology solution, which is a software-configurable optical inspection system that necessitates prior knowledge of the shape of the surface being tested [22], [23]. Although this method is a single-camera measurement technique and does not require a movable screen or camera, it is not applicable to measurements on unknown surfaces. Furthermore, there are some studies in monocular PMD techniques that utilize an auxiliary device to acquire the 3D coordinates of one point on the surface, which is referred to as the seed point. An iterative computation method subsequently reconstructs the surface. For example, Graves et al. developed a novel model-free iterative data processing method that employs a Coordinate Measuring Machine (CMM) to determine the 3D coordinates of one seed point and subsequently implements the PMD technique [24], [25]. Wang et al. used PSM (point source microscopy) to obtain accurate 3D coordinates of the seed points and added systematic error control to the iterative solution process of the rotationally symmetric surface, which improved the accuracy of the iterative reconstruction [26].

One inherent disadvantage of this method is the need for additional auxiliary equipment to get the 3D coordinates of the seed point, some of which is expensive.

The binocular PMD technique, which is based on the monocular PMD technique, uses a second camera to solve the height-slope ambiguity problem. The fundamental principle is to consistently search for the normal direction at the same reflection point on the mirror surface based on the data from the two cameras, thereby determining the normal vector of each reflection point. The final surface is subsequently obtained using the gradient integral reconstruction method [27]. If the data points are located on the measured surface, either the angle of the normal vector minimizes or coincides with each other from the data of the two cameras. Then the point's location on the measured surface is determined [28]. The process of dividing data points in this approach results in quantization mistakes, and the search for the stereo area is time-consuming. Another strategy is to search in one primary camera's light direction and determine the position of a secondary camera with the same normal vector, thereby determining the location of the measured surface point [29]. In addition, there are other binocular PMD techniques. For example, Zhang introduced a method that relies on screen-phase consistency. This method initially assumes that the surface points captured by the left and right cameras are normal in the same direction. It then tracks the corresponding points on the screen in reverse and solves the matching problem. The gradient values are obtained by minimizing the difference between the tracking phase and the decoding phase [30]. The search process employing phase consistency in this technique also has the disadvantage of being time-consuming. Han et al. proposed a novel iterative reconstruction approach for stereo PMD systems that avoids the requirement for a time-consuming search procedure for each pixel. However, the process still requires using an additional camera to obtain a seed point on the measured surface, similar to the approach of including an auxiliary device in the monocular PMD technique [31].

III. METHODOLOGY

The procedures for off-axis aspheric surface measurements by monocular PMD with an auto-updated seed point are shown in Fig. 1, where the red dotted box indicates the computational illustration of the auto-updated seed point in the iterative process. First, we roughly predict the initial height of the off-axis aspherical surface, which includes the minimum and maximum height of the measured surface. The middle height of the unknown measured surface can be calculated based on these values. Due to the fact that the integral algorithm reconstructs a relative height rather than an absolute height, the monocular PMD iterative surface reconstruction technique algorithm must update the height information of the overall measured surface with the heights of the seed points during each iteration. In this article, one point (either, the lowest, middle, or highest) is always taken as the target of the updated seed point in the iterative process, and the plane with the height of the lowest, middle, or highest point is taken as the initial iterative surface. Each iteration updates the height information of the reconstructed surface until it reaches the threshold value, at which point it outputs the measured surface results. Section III-A will detail this iteration strategy of the auto-updated seed point.

Additionally, the key techniques regarding PMD can be divided into three parts: system calibration, camera and screen correspondence, and surface reconstruction. The purpose of the system calibration is to obtain the coordinates of the camera imaging plane and the screen pixel points in the same coordinate system through calibration techniques, which are described in Section III-B. Then, as described in Section III-C, the fringe phase information is solved, completing the correspondence point matching between the screen and the camera. Finally, Section III-D describes the gradient data computation methods and integral reconstruction algorithms used to obtain reconstructed surfaces.

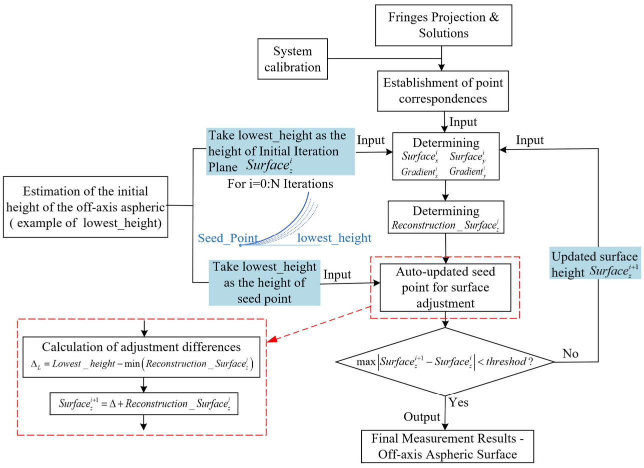

Fig. 1. Flowchart of off-axis aspheric measurement by monoscopic deflectometry with auto-updated seed point.

A. Iterative Strategy with Auto-updated Seed Point

Fig. 2 illustrates a schematic of the monocular PMD technique and shows three different seed point iteration processes. Due to the fact that the surface shape reconstructed from the gradient information is a relative surface rather than an absolute height, it is generally required to adjust the overall surface height based on the height data of a point, which can be called a seed point. The next iteration calculation uses the adjusted overall surface as its input. The proposed method always uses the one point (either, the lowest, middle, or highest) of the reconstruction off-axis aspherical surface as the seed point. It is possible to attempt any of the three strategies. Additionally, after each iteration, the reconstructed surface will undergo modifications, causing tiny changes in the 3D coordinates of the seed point. Therefore, it is necessary to update the seed point. The proposed method will automatically update the seed point, which will then serve as an input for the subsequent surface modification.

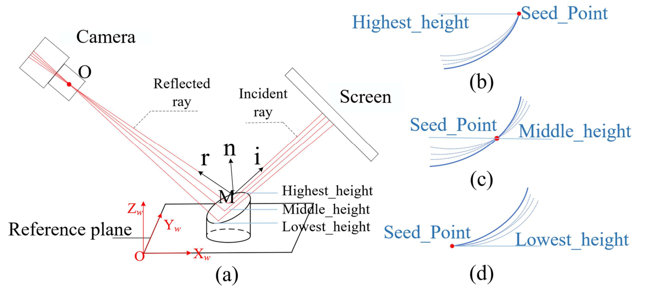

Fig. 2. Diagram of monoscopic deflectometry and three different seed point iterations. (a) monoscopic deflectometry. (b) Taking the highest point as the seed point. (c) Taking the middle point as the seed point. (b) Taking the lowest point as the seed point.

The initial height of the measured off-axis aspherical surface is roughly estimated to get the Lowest_height, Middle_height, Highest_height, which are used as target heights for the auto-updated seed point. During the adjustment process, the X and Y values are kept constant for all points on the surface in the calculation process, and only the Z values (height information) are adjusted.

Firstly, the adjustment process requires determining the difference between the seed point and the target's height, as follows:

$$\begin{cases}\Delta_L = \text{Lowest\_height} - \min\left(Reconstruction\_Surface_z^i\right),\\ \Delta_M = \text{Middle\_height} - \text{middle}\left(Reconstruction\_Surface_z^i\right),\\ \Delta_H = \text{Highest\_height} - \max\left(Reconstruction\_Surface_z^i\right).\end{cases} \tag{1}$$

where, Δ_L , Δ_M , Δ_H represent the differences in the three different strategies, respectively. $Reconstruction\_Surface_z^i$ represents the Z-value of all points on the reconstructed surface in this calculation.

Then, the difference is used to adjust all the Z-values of the reconstructed surface obtained in this iteration, as follows:

$$Surface_z^{i+1} = \Delta + Reconstruction\_Surface_z^i . \tag{2}$$

where, Δ can be any one of Δ_L , Δ_M , Δ_H . $Surface_z^{i+1}$ is the updated Z-value of all points on the surface.

Finally, the computation involves determining the difference between the Z-value $Surface_z^{i+1}$ of each point in the current outcome and the Z-value $Surface_z^i$ of the corresponding point in the prior outcome. If the maximum absolute difference between all points is less than the given threshold, the iteration ends, and the calculated surface result $\left(Surface_x^i, Surface_y^i, Surface_z^{i+1}\right)$ is output as the measured surface result. Alternatively, continue with the iteration computation, using $Surface_z^{i+1}$ as the updated surface height input.

B. System Calibration

The process of determining the coordinates of the camera's optical center, the image plane, and the pixel points on the screen in a common global coordinate system is known as system calibration. In the PMD technique, the gradient calculation through ray tracing is only feasible after the corresponding point relationship between the camera imaging plane and the screen pixels has been established. The layout of the PMD system indicates that two calibration procedures are required to determine the coordinates of the camera imaging plane and the screen pixel points, respectively. Due to the camera's inability to directly record the image displayed on the screen, it cannot be used to directly capture the checkerboard grid image on the screen for calibration. The calibration process involves indirectly establishing the conversion connection between the display and the camera by utilizing certain methods, often employing a standard plane mirror to assist in the calibration [32].

To illustrate the process of calibrating the system, the transformation relationship between the coordinate systems is shown in Fig. 3. The camera coordinate system is denoted as {C}, the screen coordinate system as {S}, the virtual screen coordinate system as {V}, and the world coordinate system as {W}. The capital letters R and T denote the rotation matrix and translation vector, respectively. The subscripts indicate the coordinate transformation between the original and target coordinate systems. For example, Rw2c denotes the rotation matrix from the world coordinate system {W} to the camera coordinate system {C} as a 3×3 matrix, and Tw2c denotes the translation vector from the world coordinate system {W} to the camera coordinate system {C} as a 1×3 vector.

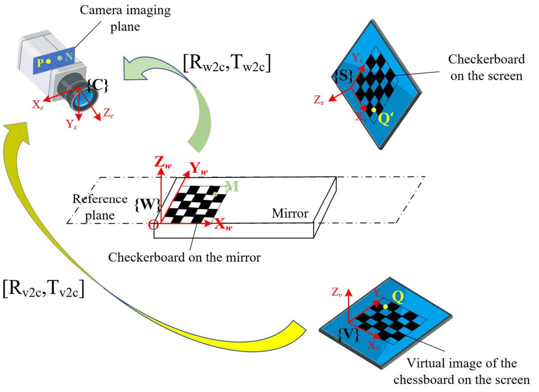

Fig. 3. Translation relationships between coordinate systems during system calibration.

Assume that a target point on the reference plane is imaged by a camera pixel $N(u_n, v_n)$; a target point $Q'\left(x_q', y_q', z_q'\right)$ on the screen is virtually mirrored in a plane mirror as $Q\left(x_q, y_q, z_q\right)$ and imaged by a camera pixel $P\left(u_p, v_p\right)$. The global attitude estimation technique allows for the estimation of both internal and exterior parameters by minimizing the reprojection of the target [33]. Here, the calibration process of camera internal and external parameters is done through taking multiple images of the calibration plate with special corner points of Zhang's camera calibration method. The internal parameters represent the radial and tangential distortions caused by the camera's intrinsic characteristics, which can distort the image. In general, to obtain a stable solution with calibration parameters, it is not necessary to consider too much higher-order aberration parameters, instead, the camera's aberration model can be appropriately simplified. The paper adopts the more commonly used Zhang's plane calibration method, in which only the more influential radial distortion is compensated in the image, and the tangential distortion is ignored [34]. It should also be noted that both the calibration plate image and the acquired image from the actual measured part need to be compensated.

Denoting the nonlinear mathematical function as $\Re$, the estimation of the reprojection error can be expressed as:

$$\begin{cases}\left[A_{v2c}\ R_{v2c}\ T_{v2c}\right] = \arg\min\sum\left\|P-\Re(Q)\right\| \\ \left[A_{w2c}\ R_{w2c}\ T_{w2c}\right] = \arg\min\sum\left\|N-\Re(M)\right\|\end{cases}. \quad (3)$$

where, A_{v2c} , A_{w2c} are intrinsic parameters of the camera R_{v2c} and T_{v2c} denote the rotation matrix and translation vector of the coordinate system {V} to {C} , respectively; R_{w2c} and T_{w2c} denote the rotation matrix and translation vector of the coordinate system {W} to {C}, respectively.

The transformation relationship between {C}, {W} and {V} for a point coordinate in different coordinate systems is shown in (4):

$$\left[X_c\ Y_c\ Z_c\ \ 1\right]^{\mathrm{T}} = M_{w2c}\left[X_w\ Y_w\ Z_w\ \ 1\right]^{\mathrm{T}} = M_{v2c}\left[X_v\ Y_v\ Z_v\ \ 1\right]^{\mathrm{T}}. \quad (4)$$

where, $\left[X_c\ Y_c\ Z_c\right]^{\mathrm{T}}$ are the coordinate of a point of the camera's image plane in the camera coordinate system {C}, and the value of Z_c is the focal length of the camera lens f; $\left[X_w\ Y_w\ Z_w\right]^{\mathrm{T}}$ is the corresponding point's coordinate in the world coordinate system {W}; $\left[X_v\ Y_v\ Z_v\right]^{\mathrm{T}}$ is the corresponding point's coordinate in the virtual screen coordinate system {V}, where $Z_v = 0$; The external parameter matrix of the coordinate system {W} to {C} is denoted as $M_{w2c} = \begin{bmatrix} R_{w2c} & T_{w2c} \\ 0 & 1 \end{bmatrix}$; The external parameter matrix of the coordinate system {V} to {C} is denoted as $M_{v2c} = \begin{bmatrix} R_{v2c} & T_{v2c} \\ 0 & 1 \end{bmatrix}$.

Therefore, based on the above correspondence, the coordinates of all the pixel points on the camera's imaging plane in the world coordinate system {W} can be determined as $\left[X_{cw}\ \ Y_{cw}\ \ Z_{cw}\right]^{\mathrm{T}}$, and the coordinates of all the pixel points on the virtual screen in the world coordinate system {W} can be determined as $\left[X_{vw}\ \ Y_{vw}\ \ Z_{vw}\right]^{\mathrm{T}}$, as shown in (5).

$$\begin{cases}\left[X_{cw}\ Y_{cw}\ Z_{cw}\ \ 1\right]^{\mathrm{T}} = inv(M_{w2c})\left[X_c\ Y_c\ Z_c\ \ 1\right]^{\mathrm{T}} \\ \left[X_{vw}\ Y_{vw}\ Z_{vw}\ \ 1\right]^{\mathrm{T}} = inv(M_{w2c})M_{v2c}\left[X_v\ Y_v\ Z_v\ \ 1\right]^{\mathrm{T}}\end{cases}. \quad (5)$$

In addition, the coordinates of the optical center of the camera lens in the world coordinate system {W} can be denoted as $\left[X_{ow}\ \ Y_{ow}\ \ Z_{ow}\right]^{\mathrm{T}}$, which is calculated by (6).

$$\left[X_{ow}\ Y_{ow}\ Z_{ow}\ \ 1\right]^{\mathrm{T}} = inv(M_{w2c})\left[0\ 0\ 0\ 1\right]^{\mathrm{T}}. \quad (6)$$

According to the relationship between virtual mirror and entity, the coordinates $\left[X_{sw}\ \ Y_{sw}\ \ Z_{sw}\right]^{\mathrm{T}}$ of the pixel points of the screen in the world coordinate system {W} can be obtained from (7).

$$\left[X_{sw}\ Y_{sw}\ Z_{sw}\right]^{\mathrm{T}} = \left[X_{vw}\ Y_{vw}\ \text{-}Z_{vw}\right]^{\mathrm{T}}. \quad (7)$$

At this point, the specific spatial location of the optical center of the camera lens, each pixel on the imaging surface, and the pixels on the screen can be determined in the world coordinate system, completing the calibration process. This gives a coordinate base for solving the measured surface gradient by using the geometrical relationship between the camera pixel points, the screen in-phase pixel points that go with them, and the measured surface reflection points. And all subsequent calculations are performed in the same world coordinate system {W}.

C. Correspondence of Camera and Screen

The process of establishing the correspondence between camera and screen pixels is shown in Fig. 4. The camera captures the deformed fringes reflected from the measured surface after sequentially displaying the horizontal and vertical phase-shifted fringes on the screen. Then the phase demodulation algorithm is used to obtain the absolute phase, which is compared with the original absolute phase of the fringes displayed on the screen to establish the corresponding correspondence.

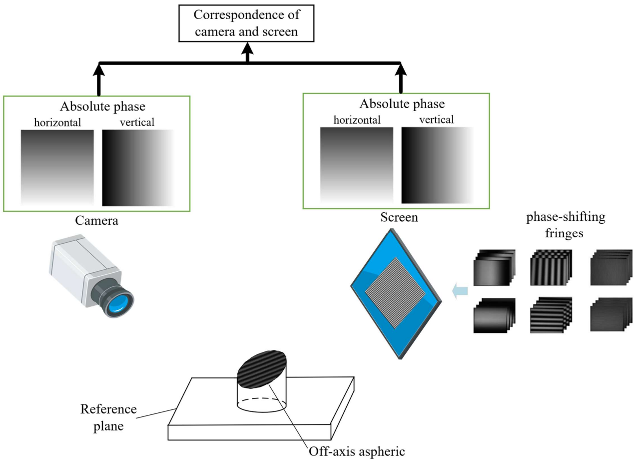

Fig. 4. Establishment of point correspondences.

The phase shift algorithm is capable of accurately determining the phase value of each individual pixel, making it a crucial component of PMD technology. The fundamental concept of phase shift involves determining the initial phase value that contains three-dimensional information about the measured surface by capturing multiple images of the fringes with a certain phase shift [35]. Several phase-shifting methods have been proposed, and this article utilizes a four-step phase shifting method considering both computing speed and accuracy [36]. Assuming that the light intensity of the fringe image is a standard sinusoidal distribution, the light intensity distribution function is:

$$I(x,y)=a(x,y)+b(x,y)\cos\left[\varphi(x,y)+\delta\right]. \tag{8}$$

where, I is the brightness of the captured image; a and b are the background and modulated light intensity, respectively; $\varphi(x,y)$ is the phase of the sinusoidal fringe that is to be identified; δ is the amount of phase shift.

The phase-solving procedure is conducted using four sinusoidal fringe patterns with phase shifts of 0, π/2, π, and 3π/2, respectively. If it represents these four fringe patterns as I_1, I_2, I_3, and I_4, the phase-solving equation is:

$$\varphi(x,y)=\arctan\frac{I_4-I_2}{I_1-I_3}. \tag{9}$$

The phase $\varphi(x,y)$ calculated by the phase shift algorithm is unique within a phase period. However, multiple fringes within the entire image will distribute the phase in a jagged pattern, necessitating the expansion of the resulting phase to obtain a continuous absolute phase value $\phi(x,y)$.

Phase unfolding technique is also a key issue in the field of phase measurement, with several accessible algorithms for phase unfolding [37]. This article chooses the multi-frequency heterodyne method for phase unfolding calculations due to its superior stability and accuracy. The method involves generating a number of phase-shifted fringe maps with different frequencies, solving for a phase value for each group of frequencies, and then superimposing the wrapped phases ϕ_1 and ϕ_2 of two frequencies λ_1 and λ_2, to obtain the phase ϕ_{12} of the other frequency λ_{12}. The frequency relationship is:

$$\lambda_{12}=\frac{\lambda_1\lambda_2}{\lambda_1-\lambda_2}. \tag{10}$$

The phase expansion is performed using fringes of three frequencies, 1/70, 1/64 and 1/59, with corresponding phases of ϕ_1, ϕ_2 and ϕ_3, respectively [38]. Using the principle of heterodyne principle, phase ϕ_{12} and phase ϕ_{23} with frequencies λ_{12} and λ_{23} are obtained by superimposing (ϕ_1, ϕ_2) and (ϕ_2, ϕ_3), respectively. According to (10), it is known that λ_{12} and λ_{23} are 1/6 and 1/5 respectively. Then, the phases with frequencies λ_{12} and λ_{23} are superimposed to obtain a phase with only one period in the whole field, which has the frequency of $\lambda_{123}=1$. This example is shown in Fig. 5. The three-frequency heterodyne method requires less accuracy in terms of the initial phase value, and the dephasing process is more stable.

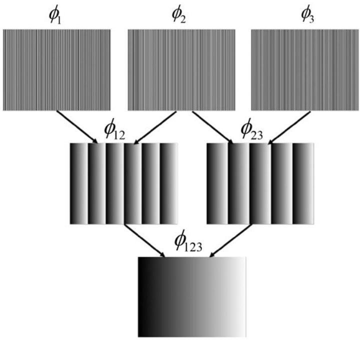

Fig. 5. Three-frequency phase expansion.

The solution of absolute phase must be performed for both horizontal and vertical fringe sets, respectively. After completing the phase-solving and unfolding procedures, a corresponding relationship is established by traversing the absolute phase obtained from the solving process and the absolute phase result generated from the screen. Once the solving and corresponding results of the horizontal and vertical fringes satisfy simultaneous consistency, the corresponding point matching between the screen and the camera pixel points is completed.

D. Surface Reconstruction

After calibrating the system to unify all coordinates to the world coordinate system {W} and determining the corresponding point relationships between the screen and camera pixel points, the slopes of the x and y directions of the points on the measured surface can be calculated. As shown in Fig. 2, according to the reflection theory, the normal vector n of the point M on the surface can be calculated by (11):

$$n=[n_x\ n_y\ n_z]^{\mathrm{T}}=r+i=[r_x{+}i_x\ r_y{+}i_y\ r_z{+}i_z]^{\mathrm{T}}. \tag{11}$$

Then, the x-gradient and y-gradient of the point M, denoted as g_x and g_y, respectively [39], can be calculated by (12).

$$\begin{cases} g_x=-\dfrac{n_x}{n_z}=-\dfrac{r_x+i_x}{r_z+i_z}=-\dfrac{\dfrac{x_C-x_M}{d_{C2M}}+\dfrac{x_S-x_M}{d_{S2M}}}{\dfrac{z_C-z_M}{d_{C2M}}+\dfrac{z_S-z_M}{d_{S2M}}} \\ g_y=-\dfrac{n_y}{n_z}=-\dfrac{r_y+i_y}{r_z+i_z}=-\dfrac{\dfrac{y_C-y_M}{d_{C2M}}+\dfrac{y_S-y_M}{d_{S2M}}}{\dfrac{z_C-z_M}{d_{C2M}}+\dfrac{z_S-z_M}{d_{S2M}}} \end{cases}. \tag{12}$$

where, x_M, y_M and z_M are the 3D coordinates of the measured surface point M. x_M and y_M can be obtained by finding the intersection of the line connecting the center of the camera lens and the pixel point of the imaging plane, with the initial plane or the iterative surface, and z_M is determined by the inputs from the initial plane or the iterative process; x_C, y_C

and z_C are the coordinates of the optical center O of the camera lens; x_S , y_S and z_S are the coordinates of the corresponding pixels on the screen; d_{C2M} is the distance from M to the optical center O of the camera and d_{S2M} is the distance from M to the screen pixel point.

Theoretically, the resulting gradient value should be equal to the partial derivatives of its 3D surface function $z(x,y)$ in both the x and y directions, as in the following (13):

$$\begin{cases} g_x(x,y) = \dfrac{\partial z(x,y)}{\partial x} \\ g_y(x,y) = \dfrac{\partial z(x,y)}{\partial y} \end{cases} . \tag{13}$$

where, $g_x(x,y)$ and $g_y(x,y)$ are the gradients in the x and y directions.

The Zernike polynomial is a high-accuracy optical wavefront fitting method that is crucial in optics [40], [41]. In this article, the Zernike polynomial is employed to fit an unknown surface and perform surface reconstruction using the gradient integral. It should be noted that Zernike polynomials are commonly used to describe optical surface errors for circular apertures due to their orthogonality on the unit circle. For non-circular apertures, the Zernike polynomials might not be applicable unless it is processed by the Gram-Schmidt (GS) orthogonalization method [42], [43]. The 37 Zernike polynomials are utilized to fit the surface of a circular off-axis paraboloid (OAP) in this work.

For convenience of calculation, the Zernike polynomial is expressed in the Cartesian coordinate system:

$$z(x,y) = a_1 Z_1(x,y) + a_2 Z_2(x,y) + \cdots + a_n Z_n(x,y) = \sum_{k=1}^{n} a_k Z_k(x,y) \cdot \tag{14}$$

where, $z(x,y)$ is the surface function, $Z_k(x,y)$ is the representation of the k-th Zernike polynomial in the Cartesian coordinate system, and a_k is the k-th coefficient.

The relationship matrix between the gradient data and partial derivatives was established to obtain the following matrix relationship (15) [44]:

$$G = \begin{bmatrix} g^x(1) \\ \vdots \\ g^x(m) \\ g^y(1) \\ \vdots \\ g^x(m) \end{bmatrix} = \begin{bmatrix} Z_1^x(1) & Z_2^x(1) & \cdots & Z_{n-1}^x(1) & Z_n^x(1) \\ \vdots & \vdots & \vdots & \vdots & \vdots \\ Z_1^x(m) & Z_2^x(m) & \cdots & Z_{n-1}^x(m) & Z_n^x(m) \\ Z_1^y(1) & Z_2^y(1) & \cdots & Z_{n-1}^y(1) & Z_n^y(1) \\ \vdots & \vdots & \vdots & \vdots & \vdots \\ Z_1^y(m) & Z_2^y(m) & \cdots & Z_{n-1}^y(m) & Z_n^y(m) \end{bmatrix} \begin{bmatrix} a_1 \\ a_2 \\ a_3 \\ \vdots \\ a_{n-1} \\ a_n \end{bmatrix} = Aa \ . \tag{15}$$

where, G is the matrix of gradient data obtained from measurements; m is the number of sampling points; n is the number of terms of the Zernike polynomial; and $Z_x^x(m)/Z_n^x(m)$ is the partial derivative of the n-th Zernike polynomial in the x/y direction at the m-th sampling point.

The coefficients of the Zernike polynomials can be determined by solving (16) with the least squares method:

$$a = \left(A^{\mathrm{T}} A\right)^{-1} \left(A^{\mathrm{T}} G\right) \cdot \tag{16}$$

After determining the polynomial coefficients, the reconstructed surface function $z(x,y)$ is obtained by substituting (14). Due to Zernike's first term $Z_1(x,y)=1$, a_1 cannot be obtained in the absence of initial conditions, and this term represents the amount of translation of the surface as a whole and does not affect the shape itself. That is, the reconstruction is of a relative surface rather than an absolute height. In the iterative approach described in this article, the Zernike first term represents one of the differences Δ_L, Δ_M , or Δ_H mentioned in Section III-A. It is used to update the surface-height information during the iteration process. The $z(x,y)$ corresponds to the Z-value $Reconstruction\_Surface_z^i$ for all points of the reconstructed surface introduced in Section III-A. It is taken into (2) to get the updated z-values $Surface_z^{i+1}$ of all the points on the surface, which is used as input to update the x and y coordinates of the surface and taken into (12) for the loop iteration procedure.

IV. EXPERIMENTAL VALIDATION

A. Setup

In this article, a measurement experiment on an off-axis aspherical mirror is performed to evaluate the feasibility and error of the proposed method. The experimental setup is shown in Fig. 6, where the key equipment is a camera (FLIR Blackfly S BFS-U3-50S5, with a lens of 6 mm focal length mounted) and a screen (size 10.1 inches with a resolution of 1024×600). They are fixed on a constructed aluminium framework. The proposed method is based on the technique of monocular camera and only one camera's data needs to be processed in the experiment. Additionally, the camera-connected PC acquires the fringe images of the measured off-axis aspheric, while the monitor-connected PC generates the fringe maps. Of course, one PC can also perform both tasks.

The measured off-axis aspherical mirror used in the experiment has an aperture of 30 mm and is one part of a paraboloid, as shown in Fig. 6. The parameters of the surface are shown in (17):

$$\begin{cases} z(x,y) = \dfrac{c\left(x^2+y^2\right)}{2} \\ \left(x \pm \delta\right)^2 + y^2 \le \left(\phi/2\right)^2 \end{cases} . \tag{17}$$

where, vertex curvature $c = 1/400$, off-axis amount $\delta = 75mm$, aperture $\phi = 30mm$, the second part of the equation $\left(x \pm \delta\right)^2 + y^2 \le \left(\phi/2\right)^2$ is the qualification that indicates an off-axis aspherical surface, and taking δ positive or negative has no effect on the surface shape.

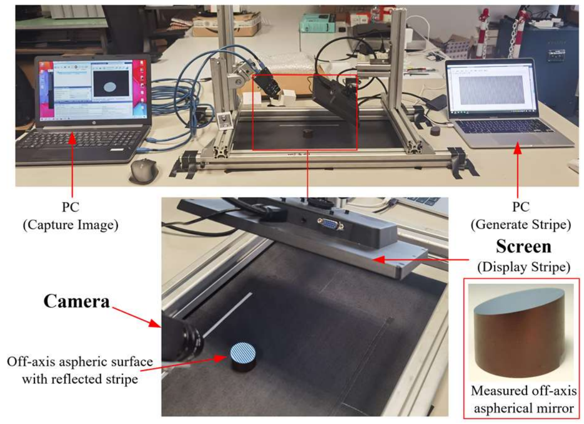

Fig. 6. Experimental setup.

B. Experiments and Results

According to the calibration method introduced in Section III-B, the coordinates of the camera optical center, the imaging surface, and the screen pixel points under the world coordinate system based on the reference surface are obtained, respectively, as shown in Fig. 7. The camera's optical center and imaging surface are approximately 120 mm away from the reference surface, and the screen's distance from the reference surface is between 48 and 90 mm.

The process involves determining the matching points between the camera and screen pixels using a three-frequency, four-step phase shift method. This is done by displaying four phase-shifted fringe maps on the screen, each with frequencies of 1/70, 1/64, and 1/59. Specifically, there are 12 fringe maps in both the horizontal and vertical directions, resulting in a total of 24 fringe maps. Additionally, the camera sequentially acquires 24 deformation fringe maps that are reflected by the measured off-axis aspherical surface. Fig. 8(a) and (b) show a certain deformed fringe map in the horizontal and vertical directions obtained by reflection, respectively. Fig. 8(c) and (d) show the absolute phases extracted from the horizontal and vertical fringes, respectively. When the extracted absolute phase matches the screen's original absolute phase in both horizontal and vertical directions, the matching process is complete.

The proposed method necessitates an approximate estimation of the height of the one point (either, the lowest, middle, or highest) of the measured off-axis aspherical workpiece. In the experiment, ordinary vernier calipers (Precision: 0.02mm) were employed to measure the height of the measured component, and it can be obtained that the rough minimum and maximum heights are 22±0.02 mm and 16.38±0.02 mm, respectively, and the middle height value of which is half of the summation of them, 19.19±0.02 mm, as shown in Fig. 9.

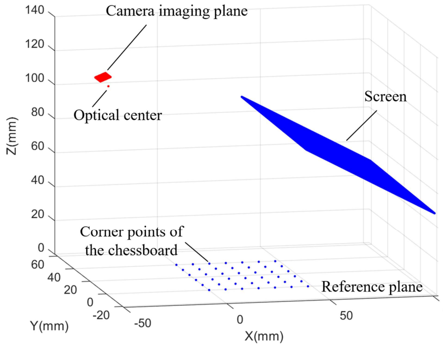

Fig. 7. Calibration results.

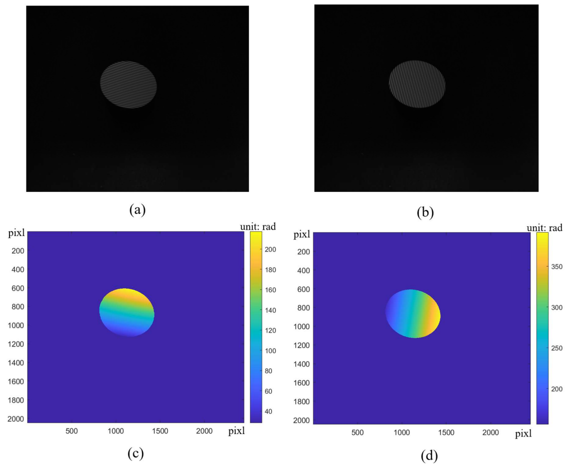

(a) (b) (c) (d)

Fig. 8. Captured images and retrieved global phase. (a) Horizontal fringe. (b) Vertical fringe. (c) Horizontal phases (d) Vertical phases.

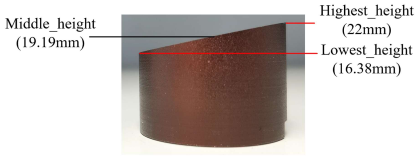

Fig. 9. Approximate estimation of the height for the measured off-axis aspherical mirror.

In the experiments, the one point (either, the lowest, middle, or highest) of the reconstructed surface is used as the auto-updated seed point, and the Lowest_height, Middle_height, or Highest_height are regarded as the target heights of the auto-updated seed point, respectively. The measurement error results of all three iterative strategies are displayed and compared with the benchmark to comprehensively evaluate the accuracy of the proposed method.

The off-axis aspherical mirror in the experiment was machined by the Precitech single-point diamond lathe (Nanoform 700, ultra, USA), and the full-surface shape errors were measured by a non-contact 3D shape measurement profiler (LUPHOScan600 LL). This non-contact profiler utilizes multi-wavelength interferometric technology and has multiple axes of motion (R, Z, C and T axes), which enables high-accuracy, full-surface form measurements of a variety of optics such as aspheric, diffractive and free-form surfaces. And its measurement accuracy of surface form error is

PV<λ/20 (λ=632.8 nm), RMS can be as small as 5 nm, and repeatability accuracy is 10 nm (600mm diameter with 150kg load). Due to the damage in the edge area of the machined part, an area with a diameter of 25 mm was selected for the full surface measurement. The physical diagram of the measurement is shown in Fig. (a). The results of the surface topography are shown in Fig. (b), with a surface form error (PV=0.658 µm and RMS=0.06 µm).

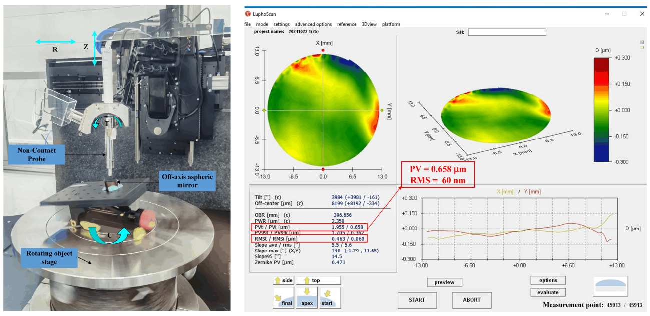

(a) (b)

Fig. 10. LUPHOScan measurement and its results. (a) Physical diagram. (b) Surface topography and form error results.

In the experiments, the difference (threshold) between the reconstructed surface of the neighboring iteration calculations is less than 1 µm as the condition for stopping the iteration. According to the three iterative strategies proposed in this article, the iterative process, the final reconstructed surface map and the error map are shown in Fig. 11. As shown in Fig. 11(a)-(c), the three iterative strategies stop the computation after the 5th, 4th, and 4th iterations, respectively; Fig. 11(d)-(f) show the output surface results of the three iterative strategies, respectively; and Fig. 11(g)-(i) show the error maps results from the three iterative strategies, respectively. The surface error data are as shown in Table 1 with results when the error value of the initial height is zero.

In addition, it is worth mentioning that in this article, it is necessary to compare the point cloud data of the output reconstructed surface with the point cloud data of the ideal surface generated by MATLAB according to the (17), to obtain the error results. The process of obtaining the error results is shown in Fig. 12. Due to the arbitrary placement of the measured off-axis aspherical surface in the world coordinate system, it is not possible to directly achieve the position results in agreement with the ideal surface, as shown in Fig. 12(a). Four points (A, B, C, D) of the reconstructed surface and four points (A', B', C', D') of the ideal surface are selected for rough registration, respectively, and the point cloud of the reconstructed surface is moved to the location where the ideal surface is located, as shown in Fig. 12(b). The ICP algorithm then performed the fine registration to continue moving the point cloud of the reconstructed surface, as shown in Fig. 12(c). Because the reconstructed surface's point cloud is not as regular as the generated ideal point cloud, it is currently not possible to directly acquire error data. It is necessary to input the X and Y data in the coordinates of the point cloud into (17) after fine registration to obtain the ideal point cloud data, Point_ideal, for comparison. Finally, the point cloud of the reconstructed surface after fine registration is compared with Point_ideal as shown in Fig. 12(d), and the error map is shown in Fig. 12(e).

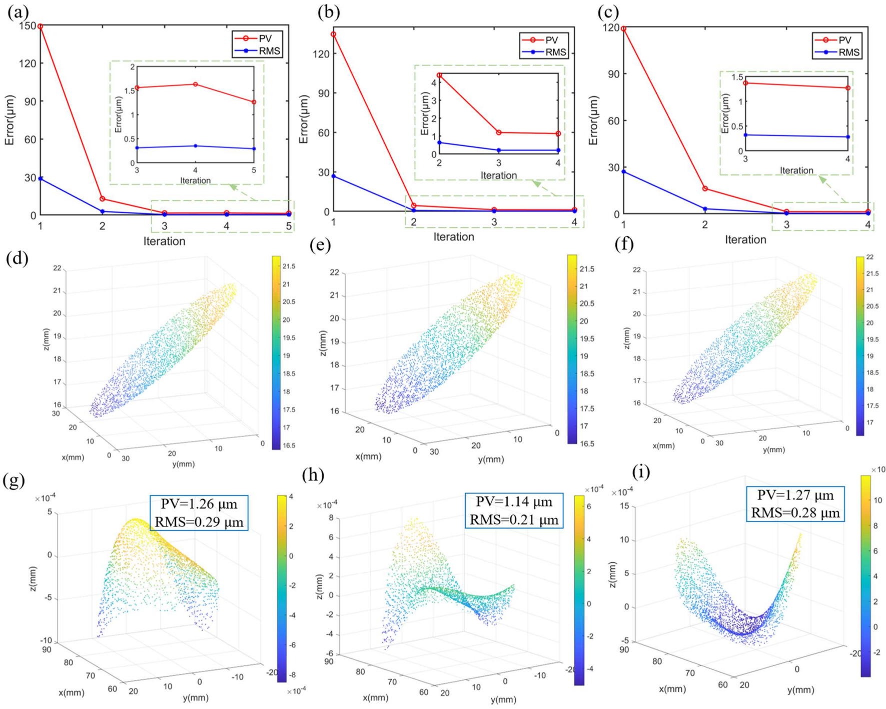

Fig. 11. Measurement results of the proposed method. (a)-(c) Process of iterations with Lowest_height, Middle_height and Highest_height as iterative strategies, respectively. (d)-(f) Output surface results with Lowest_height, Middle_height and Highest_height as iterative strategies, respectively. (g)-(i) Error maps with Lowest_height, Middle_height and Highest_height as iterative strategies, respectively.

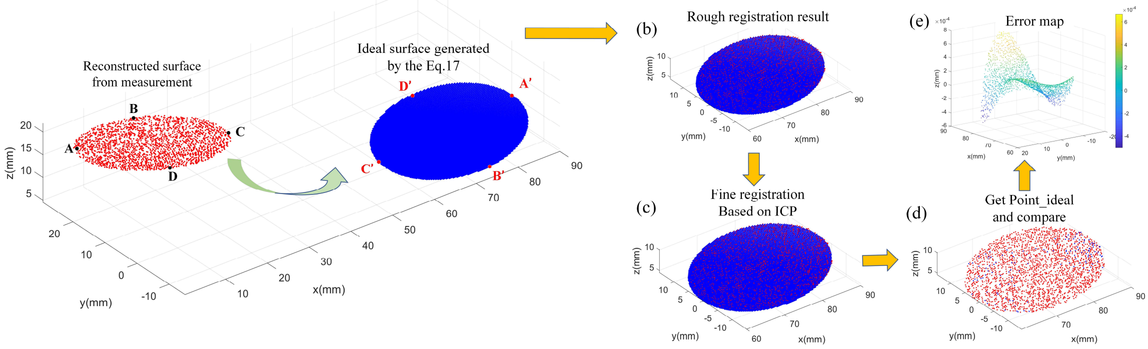

Fig. 12. The process of acquiring error map. (a) The reconstructed surface from measurement and the ideal surface generated by Eq.17. (b) Rough registration. (c) Fine registration. (d) Comparison between the measured surface point cloud and the ideal point cloud (Point_ideal). (e) Error map.

Therefore, in order to assess the measurement accuracy of the proposed method in an optimal way, the measurement results of the LUPHOScan600 LL were used as a benchmark and compared with the results obtained from the error solving process shown in Fig. 12 to obtain the measurement error of the proposed method, which corresponds to the data with an initial height of 0 in Table 1. The deviations of the PV values are all less than 1 μm; the deviations of the RMS are less than 0.3 μm. It demonstrates that the proposed method is highly accurate.

C. Evaluation for Impact of Initial Height Error

In this article, ordinary vernier callipers with a precision of 0.02 mm were employed to measure the height of the measured components. However, this approach may introduce certain errors when estimating the initial height. The estimated lowest, middle and highest heights should bein the range of 16.38±0.02mm, 19.19±0.02mm and 22±0.02mm respectively. In three different iterative strategies, the auto-updated seed point heights with limiting errors are employed in the proposed method, respectively.

To comprehensively evaluate the impact of the initial height error on the measurement results, all the error results were compared with the benchmark. The evaluation results are shown in Table 1. Comparison of the results shows that the maximum deviation of the PV value is 1.04 μm and the maximum deviation of the RMS value is 0.35 μm. It can be concluded that even the initial height error obtained from an ordinary vernier caliper has little effect on the measured surface shape, since it only leads to a small offset in the whole surface location.

In addition, it can be seen from Table 1 that there are certain trends and regularity. The measurement results are better (closer to the benchmark) when Middle_height is used as the initial height.The two results with the largest errors occur at 16.36 and 22.02, which means that at the positions of the limit values at both ends makes the larger errors. Therefore, it should be avoided to use the limit values at both ends as the initial height for the calculation in the application, but try to use the Middle_height or the height with its limit value for the calculation. When it is not possible to use the middle point, it can also use Lowest_height or Highest_height without the limit values of the both ends for calculation.

TABLE I

ACCURACY EVALUATION OF THE PROPOSED METHOD

Height of auto-updated seed point(mm)	Error of initial height(mm)	Error map(μm) PV	Error map(μm) RMS	Difference with Benchmark(μm) PV	Difference with Benchmark(μm) RMS
Lowest_height 16.38	+0.02	1.22	0.27	0.56	0.21
	0	1.26	0.29	0.60	0.23
	-0.02	1.70	0.39	1.04	0.33
Middle_height 19.19	+0.02	1.11	0.29	0.45	0.23
	0	1.14	0.21	0.48	0.15
	-0.02	1.20	0.30	0.54	0.24
Highest_height 22	+0.02	1.58	0.38	0.92	0.32
	0	1.27	0.28	0.61	0.22
	-0.02	1.26	0.32	0.60	0.26

Benchmark - Measurement result of Talysurface PGI 3D (μm): PV=0.66 RMS=0.06

V. DISCUSSION

1) Novelty and low-cost vs. prior approaches**:** Existing monocular PMD methods either require moving the screen or camera to complete the measurement process twice, or requiring other equipment (e.g., CMM, Point Source Microscope) to obtain the exact 3D coordinates of the seed point that is employed during the iterative process. However, in the proposed monocular PMD method, the accuracy requirement of the seed point is reduced by the strategy of automatic updated seed point, and only a rough measurement by vernier caliper is needed to obtain the lowest, middle, or highest point on the measured mirror, which is used as the height information Z of the seed point being kept unchanged while the (X,Y) of the seed point is continuously updated during iteration. Then, Z1 of the Zernike polynomials is associated with the height information Z of the seeds to complete the iterative optimization process using Zernike polynomial fitting and rebuild the surface based on the slope data. In this way, it is possible to achieve micrometer-level measurement accuracy by low-cost means through the strategy of auto-updated seed point and the rough estimation of height information using vernier calipers. Of course, other cost-effective methods for estimating the initial height can be utilized to obtain the same results.

2) Limitations of the proposed method**:** Furthermore, this

method selects the one of unique and valid feature points (either, the lowest, middle, or highest) on the reconstructed off-axis aspherical surface as the target of the automatic seed point update during the iterative computation. Then, the overall surface can be restored to its actual height by adjusting the surface height, which is helpful for the convergence of the iterative process. However, it is difficult to identify the unique lowest or highest point of a rotationally symmetric surface (e.g. a full aspherical surface). Therefore, the proposed method also has some limitations that are not applicable to rotationally symmetric surfaces, but applicable to non-rotationally symmetric surfaces with valid feature points, such as off-axis aspherical surfaces. Nevertheless, the proposed method may provide a reference for solving the measurement challenges of complex optical elements, such as free-form surfaces with equivalent available feature points.

3) Future work**:** In this work, a surface type fitting and experimental validation of the OAP has been carried out using Zernike polynomials, which is only applicable to circular aperture. It is possible to try different polynomial fitting methods to obtain different results in the future. It can be attempted different polynomial fitting methods to achive different results can be used. For example, it can be generalized to Chebyshev polynomials [45], or Zernike polynomials with Gram-Schmidt (GS) orthogonalization for non-circular apertures [42], [43], which can measure discontinuous surfaces and enables fitting surfaces using slope data. For surface error fitting with higher frequencies, the recursive Zernike polynomial algorithm could also be used [46]. In terms of the improvement of measurement accuracy, there is still potential improvement of the work in this paper in the future. Firstly, based on the strategy of automatic updated seed points proposed in this paper, it can adopt different ways in the system calibration and surface reconstruction to get a more comprehensive comparison of the results, so that a new approach could be found to improve the measurement accuracy. Meanwhile, the accuracy of the OAP component in this work has not reached the sub-micron level due to the limitation of the experimental conditions, and the current work can only achieve the micron level measurement accuracy. In the future, it is possible to experimentally validate a higher accuracy based on the adoption of new means in the key processes and sub-micron surface of measured workpieces.

VI. CONCLUSION

In this article, a novel strategy with auto-updated seed points during the iteration process is proposed for off-axis aspherical surface measurement based on monocular PMD technology. Compared with the prior literature, the advantage of this method is that it reduces the requirement of seed point accuracy during the iterative process, and only requires rough measurements of the heights of the lowest and highest points of the measured off-axis aspherical mirrors by using affordable tools such as vernier calipers, which achieves a high measurement accuracy in a cost-effective way. The experimental part also comprehensively evaluates the effect of initial height error on the measurement results. Comparing the results with the results of a high-precision profilometer, it can be concluded that the proposed method can achieve micron-level measurement accuracy. The proposed method is simpler, less costly and more effective, avoiding the complex operations of camera and screen movement or the high cost of auxiliary equipment in the existing monocular PMD technique, as well as the time-consuming consistency matching calculations in the binocular PMD technique. It will also provide some references for solving the difficult problem of measuring complex optical components (e.g. free-form surfaces with similar feature points) in the future.

REFERENCES

[1] X.J. Zhang, et al., “Challenges and strategies in high-accuracy manufacturing of the world's largest SiC aspheric mirror,” *Light: Science & Application*, vol. 11, no. 1, Oct. 2022, Art. no. 310.

[2] F.Y. Wang, et al., “A Machine Vision Method for Correction of Eccentric Error Based on Adaptive Enhancement Algorithm,” *IEEE Transactions on Instrumentation and Measurement*, vol. 70, Mar. 2021, Art. no. 5002311.

[3] J.Y. Han, S. Lee, “Methods of defining circular off-axis aspheric mirrors,” *Journal of Astronomical Telescopes, Instruments, and Systems*, vol. 4, no. 4, Oct. 2018, Art. no. 044002.

[4] T. Yang, D.W. Cheng, Y.T. Wang, “Direct generation of starting points for freeform off-axis three-mirror imaging system design using neural network based deep-learning,” *Optics Express*, vol. 27, no. 12, pp. 17228–17238, Jun. 2019.

[5] A. Witze, “what’s next for the Thirty Meter Telescope? ,” *Nature*, vol. 572, no. 7769, pp. 292–293, Aug. 2019.

[6] D. Kim, et al., “Advances in optical engineering for future telescopes,” *Opto-Electronic Advances*, vol. 4, no. 6, Aug. 2019, Art. no. 210040.

[7] F.J. Chen, et al., “Profile error compensation in ultra-precision grinding of aspheric surfaces with on-machine measurement,” *International Journal of Machine Tools & Manufacture*, vol. 50, pp. 480-486, Jan. 2010.

[8] Z.X. Li, X.D. Zhang, Y. Yu, “Precise surface form measurements of off-axis aspheric freeform optics,” *Proc. of SPIE*, vol. 12765, Oct. 2023, Art. no. 127650N.

[9] Z.C. Dong, H.B. Cheng, X. Ye, H.Y. Tam, “Developing on-machine 3D profile measurement for deterministic fabrication of aspheric mirrors,” *Applied Optics*, vol. 53, no. 22, pp. 4997-5007, Aug. 2014.

[10] X.P. Guo, et al., “Contact on-machine measurement probe error correction method for optical aspheric surface ultraprecision machining,” *Measurement*, vol. 214, Mar. 2023, Art. no. 112731.

[11] G.F. Qiu, X.D. Cui, “A contact inspection system for aspheric optical components,” *Optik*, vol. 127, pp. 7572-7577, May. 2016.

[12] G. Häusler, et al., “Deflectometry vs. Interferometry,” *Proc. of SPIE*, vol. 8788, May. 2013, Art. no.87881C.

[13] W. Lang, et al., “A General Reconstruction Framework for Deflectometric Measurement Based on Nonuniform B-Splines,” *IEEE Transactions on Instrumentation and Measurement*, vol. 72, May. 2023, Art. no. 5015511.

[14] K. Mantel, et al., “Interferometric quasi-absolute tests for aspherics using a radial shear position,” *Optics Letters*, vol. 34, no.20, pp. 3178-3180, Oct. 2009.

[15] D.Y. Zhu, et al., “Research on hybrid compensation testing of convex aspherical mirror,” *Optics and Lasers in Engineering*, vol. 132, Apr. 2020, Art. no. 106108.

[16] S.Y. Chen, et al., “Testing of large optical surfaces with subaperture splicing,” *Applied Optics*, vol.46, no.17, pp. 3504–3509, Jun. 2007.

[17] Z.Q. Niu, et al., “Adaptive phase correction for phase measuring deflectometry based on light field modulation,” *IEEE Transactions on Instrumentation and Measurement*, vol. 70, Mar. 2023, Art. no. 7003610.

[18] L. Huang, et al., “Review of phase measuring deflectometry,” *Optics and Lasers in Engineering,* vol.107, pp. 247-257, Mar. 2018.

[19] J. Balzer, S. Werling, “Principles of Shape from Specular Reflection,” *Measurement*, vol. 43, pp. 1305-1317, Aug. 2010.

[20] Y. Tang, et al., “3D shape measurement of the aspheric mirror by advanced phase measuring deflectometry,” *Optics Express*, vol.16, no.19, pp. 15090-15096, Sep. 2008.

[21] Y. Tang, et al., “A novel phase measuring deflectometry for aspheric

mirror test," *Optics Express*, vol.17, no.22, pp. 19778–19784, Oct. 2009.

[22] P. Su, et al., "Aspheric and freeform surfaces metrology with software configurable optical test system: a computerized reverse Hartmann test," *Optical Engineering*, vol. 53, no. 3, Mar. 2014, Art. no. 031305.

[23] R. Huang, P. Su, et al., "Optical metrology of a large deformable aspherical mirror using software configurable optical test system," *Optical Engineering*, vol.53, no.8, Aug. 2014, Art. no. 085106.

[24] L.R. Graves, et al., "Model-free optical surface reconstruction from deflectometry data," *Proc. SPIE*, vol. 10742, Sep. 2018, Art. no. 107420Y.

[25] L.R. Graves, et al., "Model-free deflectometry for freeform optics measurement using an iterative reconstruction technique," *Optics Letters*, vol.43, no.9, pp. 2110–2113, May. 2018.

[26] R.Y. Wang, D.H. Li, X.W. Zhang, "Systematic error control for deflectometry with iterative reconstruction," *Measurement*, vol. 168, no. 108393, Jan. 2021.

[27] R.Y. Wang, et al., "Vision ray model based stereo deflectometry for the measurement of the specular surface," *Optics and Lasers in Engineering*, vol. 172, Sep. 2023, Art. no. 108731.

[28] M.C. Knauer, J. Kaminski, and G. Hausler, "Phase measuring deflectometry: a new approach to measure specular free-form surfaces," *Proc. SPIE*, vol. 5457, Sep. 2004.

[29] Y.J. Xu, F. Gao, X.Q. Jiang, "Performance Analysis and Evaluation of Geometric Parameters in Stereo Deflectometry," *Engineering*, vol. 4, pp. 806–815, Apr. 2018.

[30] H.L. Zhang, et al., "Displacement-free stereoscopic phase measuring deflectometry based on phase difference minimization," *Optics Express*, vol. 28, no. 21, pp. 31658–31674, Oct. 2020.

[31] H. Han, et al., "3D reconstruction of the specular surface using an iterative stereoscopic deflectometry method," *Optics Express*, vol. 29, no. 9, pp. 12867–12879, Apr. 2021.

[32] X.Y. Xu, et al., "Self-calibration of in situ monoscopic deflectometric measurement in precision optical manufacturing," *Optics Express*, vol. 27, no. 5, pp. 7523–7536, Mar. 2019.

[33] J. Heikkila, O. Silven, "A Four-step Camera Calibration Procedure with Implicit Image Correction," *IEEE Proceedings CVPR 97*, pp. 1106–1112, Jun. 1997.

[34] Z.Y, Zhang, "A Flexible New Technique for Camera Calibration," *IEEE Trans. Pattern Anal. Mach. Intell.*, pp. 1330–1334, Nov. 2000.

[35] Y.W. Wang, et al., "Efficient Half-Period Phase Histogram Equalization for General Phase-Shifting Algorithms with Phase Shift Errors," *IEEE Transactions on Instrumentation and Measurement*, vol. 71, Oct. 2022, Art. no. 5023810.

[36] J.H. Wang, Y.X. Yang, "Triple N-Step Phase Shift Algorithm for Phase Error Compensation in Fringe Projection Profilometry," *IEEE Transactions on Instrumentation and Measurement*, vol. 70, Sep. 2021, Art. no. 7006509.

[37] C. Reich, R. Ritter, J. Thesing, "3-D shape measurement of complex objects by combining photogrammetry and fringe projection," *Opt. Eng.*, vol. 39, no. 1, pp. 224–231, Jan. 2000.

[38] C. Reich, R. Ritter, J. Thesing, "White light heterodyne principle for 3D-measurement," *Proc. of SPIE*, vol. 3100, pp. 236–244, Jan. 1997.

[39] J.Q. Ye, et al., "In-situ deflectometic measurement of transparent optics in precision robotic polishing," *Precision Engineering*, vol. 64, pp. 63–69, Mar. 2020.

[40] K. Niu, C. Tian, "Zernike polynomials and their applications," *Journal of Optics*, vol. 24, Nov. 2022, Art. no. 123001.

[41] M. Schilke, J. Liebl, C. Wünsche, "Surface reconstruction by using Zernike Polynomials," *Proc. of SPIE*, vol. 10009, Apr. 2016, Art. no.1000910.

[42] C.Y. Zhao, J.H. Burge, "Orthonormal vector polynomials in a unit circle, Part I: basis set derived from gradients of Zernike polynomials," *Optics Express*, vol. 15, no.26, pp. 18014–18024, Dec. 2007.

[43] R. Upton, B. Ellerbroek, "Gram–Schmidt orthogonalization of the Zernike polynomials on apertures of arbitrary shape," *Optics Letters*, vol. 29, no. 24, pp. 2840–2842, Dec. 2004.

[44] D.T. Nguyen, et al., "Modal Reconstruction Based on Arbitrary High-Order Zernike Polynomials for Deflectometry," *Mathematics*, vol. 11, no. 18, Sep. 2023, Art. no.3915.

[45] M. Aftab, et al., "Chebyshev Gradient Polynomials for High Resolution Surface and Wavefront Reconstruction," *Proc. SPIE*, vol. 10742, Aug. 2018, Art. no. UNSP 1074211.

[46] B.H. Shakibaei, R. Paramesran, "Recursive formula to compute Zernike radial polynomials," *Optics Letters*, vol. 38, no. 14, pp. 2487–2889, Jul. 2013.

Menghui Lan received his BSc degree from Huazhong Agricultural University in 2014, MSc and Ph. D. degrees all from Xi'an Jiaotong University in 2017 and 2025, respectively. He is currently an assistant professor in the School of Mechanical Engineering, Xi'an Jiaotong University, China. His main research interests include interferometry and vision measurement, aspheric measurement and processing technology.

Bing Li received the Ph.D. degree from Xi'an Jiaotong University, Xi'an, China, in 2004. He is currently a Professor with the State Key Laboratory for Manufacturing Systems Engineering and the Deputy Director of the Collaborative Innovation Center of High-End Manufacturing Equipment, Xi'an Jiaotong University. His research interests include micro and nano measurements on complex surfaces.

Xiang Wei received the Ph.D. degree from Xi'an Jiaotong University, Xi'an, China, in 2018. He is currently an associate researcher with the Department of Mechanical Engineering, Xi'an Jiaotong University. His research interests include precision machining and testing of complex aspheric surfaces.

Emanuele Zappa (Senior Member, IEEE) is a Full Professor with the Mechanical and Thermal Measurements, Politecnico di Milan, Milan, Italy. His scientific activity is mainly in the field of mechanical and image-based measurement.

Dr. Zappa is an Associate Editor-in-Chief of IEEE Transaction on Instrumentation and Measurement.